Electrochimica Acta 497 (2024) 144571

Contents lists available at ScienceDirect

Electrochimica Acta

journal homepage: www.journals.elsevier.com/electrochimica-acta

A novel modeling approach for sulfurized polyacrylonitrile (SPAN) electrodes in Li metal batteries

Esther Kezia Simanjuntak [a,b], Timo Danner [a,b,*], Peiwen Wang [c], Michael R. Buchmeiser [c], Arnulf Latz [a,b,d]

[a] Institute of Engineering Thermodynamics, German Aerospace Center (DLR), Pfaffenwaldring 38-40, 70569 Stuttgart, Germany
[b] Helmholtz Institute Ulm for Electrochemical Energy Storage (HIU), Helmholtzstraße 11, 89081 Ulm, Germany
[c] Institute of Polymer Chemistry, University of Stuttgart, Pfaffenwaldring 55, 70569, Stuttgart, Germany
[d] Institute of Electrochemistry, University of Ulm, Albert-Einstein-Allee 47, 89081 Ulm, Germany

ARTICLE INFO

Keywords:
Lithium-sulfur batteries
Continuum modeling
Sulfurized poly(acrylonitrile) (SPAN)
Electrode design

ABSTRACT

Li-sulfur batteries represent a promising class of next-generation batteries with high theoretical gravimetric capacity. Moreover, the absence of scarce elements such as nickel or cobalt makes them a sustainable alternative to Li-ion batteries. However, it is well known that the main problem of Li-sulfur batteries is the so-called polysulfide shuttle, which leads to self-discharge, capacity fading and low coulombic efficiency. In recent years, several mitigation strategies have been developed for Li-sulfur batteries to reduce the polysulfide shuttle effect. One promising approach is to covalently bond the sulfur to a polymer backbone. A well-known class of materials is sulfurized poly(acrylonitrile) (SPAN), for which long cycle life and high specific capacities have been reported. In this work, we present a novel continuum model for SPAN electrodes and demonstrate its application in Li-SPAN batteries. Within our simulation framework we include both red/ox reactions of covalently sulfur on PAN as well as transport and reactions of polysulfides in the solution. By combining simulations and experimental data we analyze the discharge mechanism and provide guidelines for electrode design.

1. Introduction

The electrification of aircraft promotes the development of sustainable and low-cost rechargeable batteries with high energy density and long cycle life. In this context, sulfur as a lightweight element has been widely investigated as a cathode material for post-lithium-ion battery technology [1–3]. Compared to conventional lithium-ion batteries (LIBs), lithium-sulfur (Li–S) batteries have a significantly higher theoretical gravimetric capacity of 1672 mAh/g_S, and a theoretical specific energy density of 2500 Wh/kg_S [4]. Most importantly, sulfur is a very abundant raw material that promises to be a sustainable and low-cost alternative to LIBs, which is compelling for large-scale production.

Despite the attractive properties mentioned above, Li–S batteries are still not produced in larger scale due to several problems. The most vital challenge is the so-called polysulfide shuttle [5–7]. The dissolved polysulfide species in the electrolyte are able to diffuse to the anode and undergo parasitic side reactions [8]. This phenomenon eventually reduces the capacity, coulombic efficiency, and cycle life of the cell [9,10]. Several polysulfide retention strategies have been proposed and investigated to mitigate this shuttle effect. Most of the approaches focus on the development of new cathode materials. Generally, one can distinguish between two different strategies for polysulfide retention. The classical approach is based on the confinement of polysulfide species. During electrode preparation the sulfur is essentially impregnated in highly conductive carbon materials with micro- or mesopores. Numerous materials have been reported in the literature for this approach [7,11–16]. A second strategy involves the formation of covalent bonds between sulfur and a cathode host material. In this case, the sulfur is bound to a graphitized polymer backbone e.g., sulfurized poly(acrylonitrile) (SPAN) [11,17–29]. This approach has shown to deliver a remarkable battery cycle life as well as excellent rate performance with high coulombic efficiency (>99%). These promising results demonstrate the viability of this approach and, in particular, the potential of SPAN as cathode material in Li-SPAN cells.

In order to exploit the favorable properties of this emerging class of materials, suitable electrode and cell designs need to be developed

* Corresponding author at: Institute of Engineering Thermodynamics, German Aerospace Center (DLR), Pfaffenwaldring 38-40, 70569 Stuttgart, Germany.
E-mail address: timo.danner@dlr.de (T. Danner).
URL: http://www.dlr.de/tt/en/ (T. Danner).

https://doi.org/10.1016/j.electacta.2024.144571
Received 14 April 2024; Received in revised form 5 June 2024; Accepted 8 June 2024
Available online 11 June 2024

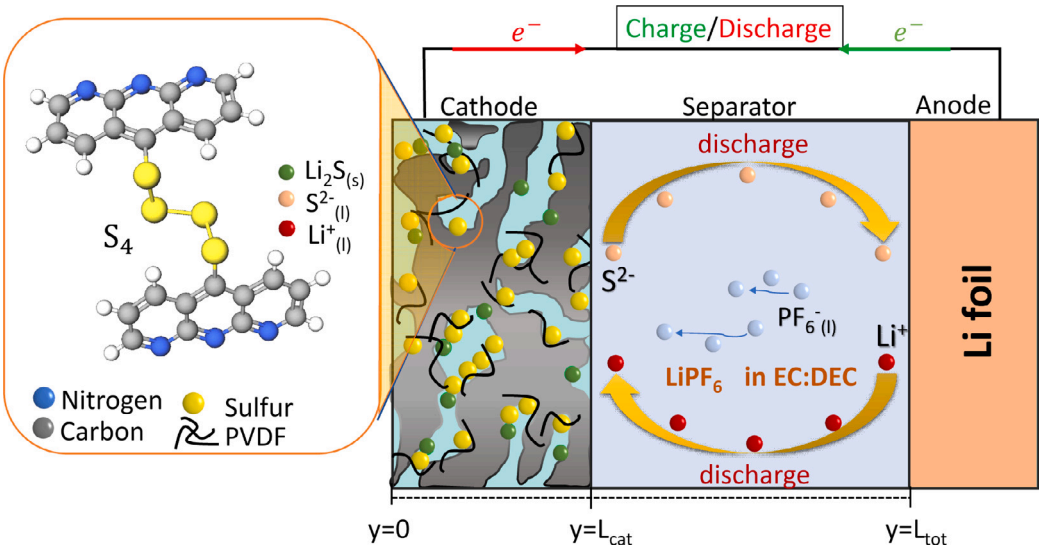

Fig. 1. Schematic of a Li-SPAN cell consisting of a SPAN/C composite cathode, glass fiber separator, and Li metal anode. Sulfur (yellow color) is bound to the polymer backbone as shown in the magnification. S^{2-} is in solution during reduction and oxidation. At the end of discharge solid Li_2S (green color) can form in the cell.

for Li-SPAN batteries. Continuum models are often used in the development of LIBs to optimize electrode design [30–34]. In recent years, several models for Li–S batteries have been reported in the literature that can provide guidelines for battery development [35–44]. Numerous atomistic investigations utilizing density functional theory (DFT) have been documented in the literature regarding SPAN material [45–49]. However, as far as we are aware, there is currently no literature on continuum models specifically addressing Li-SPAN batteries.

In this work, we present a novel approach to model Li-SPAN batteries. The model is parametrized and validated using experimental data measured on Li-SPAN coin cells. On the basis of our model, we perform first simulation studies to deduce the relevant parameters for cell design and future optimization of Li-SPAN batteries.

In Section 2 we present the derivation of the model equations. Model parameters are presented in Section 2.4 and measurements on Li-SPAN batteries are described in Section 3. Finally, the simulation results including a validation with experimental data and a parameter study providing directions for electrode development are presented in Section 4.

2. Theory

In this study, we present a novel model for the simulation of Li-SPAN batteries. In the main part of this manuscript we focus on the detailed description of the SPAN model and key assumptions. A complete description of all governing equations in our simulation framework is given in the supporting information.

2.1. General model description

A schematic of the geometry of the Li-SPAN cell is illustrated in Fig. 1. The Li-SPAN cell consists of a Li metal anode, a porous separator, and a porous cathode containing SPAN, conductive additives and binder. The cathode and separator have a thickness of L_{cat} and L_{sep}, respectively. The Li negative electrode is modeled as a metallic surface at position $L_{tot} = L_{cat} + L_{sep}$. The pore space of the cathode and separator is soaked with the electrolyte solution. In this study we simulate a common carbonate-based electrolyte comprising 1 M $LiPF_6$ in EC/DEC (1:1). In our simulations, we calculate the distributions of dissolved species, phases, and potentials within the positive electrode and the separator domain. Both chemical and electrochemical reactions take place at the electrode/electrolyte interface of the anode and cathode, respectively. The SPAN reduction mechanism is schematically illustrated in Fig. 2 and discussed in the paragraph below. Furthermore, precipitation and dissolution of solid Li_2S on the positive electrode surface and its effect on reaction and transport are considered. The transport of mass and charge in the electrolyte between the cathode and the anode is described with an extension of concentrated solution theory taking into account the diffusion and migration of S^{2-} as illustrated in Fig. 1.

2.2. SPAN reaction mechanism

SPAN as cathode material for Li–S batteries has recently been reported in several studies [11,17,19–23,23–26,26–29,50–55]. In this work we refer to the reaction mechanism of the Li-SPAN system suggested in Ref. [17,29], and [53]. The cathode material SPAN is produced by a reaction of sulfur with PAN at elevated temperatures. As a result, sulfur (S_8) is not found in elemental form as in classical Li–S batteries. Instead, sulfur is bound in the form of oligo(sulfide)s to carbon atoms in the PAN-derived backbone, which greatly reduces the issues related to the polysulfide shuttle. During discharge, S^{2-} anions are cleaved from the oligo(sulfide) chains and form Li_2S with Li^+ cations in the electrolyte. Kappler et al. [29] as well as Bertolini et al. [56] have reported that the presence of nitrogen in the carbonaceous matrix has a significant role in preventing the migration of polysulfide in the electrolyte phase. Furthermore, Klostermann et al. [53] noted that successive lithiation steps precede each detachment of Li_2S, actively impeding the cleavage of longer-chain polysulfides. The interaction between polysulfides and nitrogen allows a unique reversible redox mechanism of SPAN. Kappler et al. [29] and Warneke et al. [22] have also demonstrated that the Li-SPAN battery exhibits exceptional cycling stability with a carbonate-based electrolyte. The utilization of carbonate electrolytes, known for their low polysulfide solubility [57], facilitates the deposition of Li_2S adjacent to the PAN backbone, thereby mitigating the shuttle effect.

Fig. 2 schematically illustrates the assumed reaction mechanism. Each oligo(sulfide) chain on the PAN-derived backbone has two docking sites at the two ends of the chain. Bertolini et al. [56] has demonstrated via DFT calculation, that the motif of sulfur chain on the SPAN influences the reversibility of Li-SPAN batteries. In their work, it is proposed that the sulfur chain might have two docking sites creating

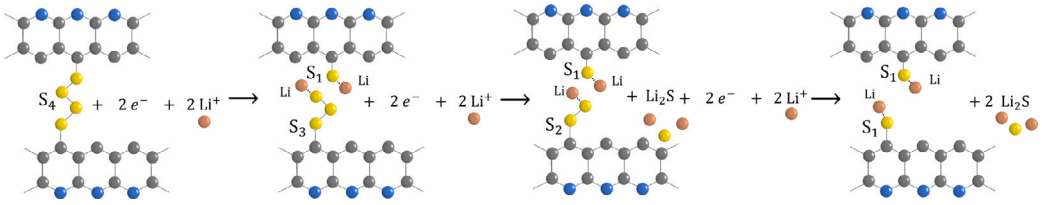

Fig. 2. Schematic of the discharge mechanism of SPAN in a Li-SPAN battery.

a bridge. However, longer sulfur chains on SPAN could result in the extraction of long polysulfide species, potentially leading to polysulfide shuttling. The length of oligo(sulfide) chains depends on synthesis conditions and can be tuned to optimize sulfur loading (long chains) or cycling stability (short chains). Therefore, different chain lengths have been reported in the literature [17,18,46,47,52,53] ranging from one to seven sulfur atoms (S_x, $1 \leq x \leq 7$) in the PAN-derived structure. The average length of the oligo(sulfide) chains is around four sulfur atoms (S_4). During the discharge process, the S_4 oligo(sulfide) chain first breaks preferentially between sulfur atoms 1 and 2. Both chain ends are immediately coordinated by lithium ions, resulting in chains of length S_3 and S_1. Upon further discharge, the S_3 oligo(sulfide) is first reduced to length S_2 and then to S_1 by cleaving an S^{2-} anion in each step. At the end of the discharge process, a sulfur atom is still to the carbon atom of the backbone structure, acting as docking site for S^{2-} anions during charging. In our simplified mechanism, S^{2-} anions are immediately coordinated by Li^+ cations in the electrolyte and eventually solid Li_2S is formed above the solubility limit of the electrolyte solution. This is in agreement with the observations by Xiaofei et al. [51], who reported a uniform coverage of their SPAN fibers with Li_2S nanoflakes at the end of the discharge. This finding is also supported by Klostermann et al. [53], who mentioned that the nucleation of Li_2S at the SPAN backbone is energetically favored via Density Functional Theory simulations. In this work, we focus on the discharge process, and a detailed discussion of the charging mechanism will be presented in future work.

2.3. Model formulation

Model formulation is explained in the upcoming sections.

2.3.1. Model framework

The model outlined in this research builds on our previous theoretical work on carbon-based Li–S batteries [6,41,43,58]. We formulate and solve fundamental conservation equations governing mass and charge of each species involved in both the electrolyte and solid phases to predict Li–S battery performance at the cell level. Through this method, we are able to track the distribution of local concentration and potential in both electrode and electrolyte phases, as well as the solid charge and discharge products. In the following sections, we provide a detailed explanation and derivation of the simulation domain, governing equations, and simulation parameters.

2.3.2. SPAN kinetic model

The SPAN reduction process follows a reaction pathway consisting of two distinct steps. First, it involves the cleavage of the oligo(sulfide) chain, which is represented as follows

$$1/2\ \text{PAN-S}_4\text{-PAN} + e^- + \text{Li}^+ \rightleftharpoons 1/2\ \text{PAN-S}_3\text{Li} + 1/2\ \text{PAN-S}_1\text{Li}\ . \tag{1}$$

Subsequently, it involves the stepwise reduction of PAN-S_3Li, yielding S^{2-} within the electrolyte solution which can be formally expressed by

$$1/2\ \text{PAN-S}_3\text{Li} + e^- \rightleftharpoons 1/2\ \text{PAN-S}_2\text{Li} + 1/2\ \text{S}^{2-}. \tag{2}$$

$$1/2\ \text{PAN-S}_2\text{Li} + e^- \rightleftharpoons 1/2\ \text{PAN-S}_1\text{Li} + 1/2\ \text{S}^{2-}. \tag{3}$$

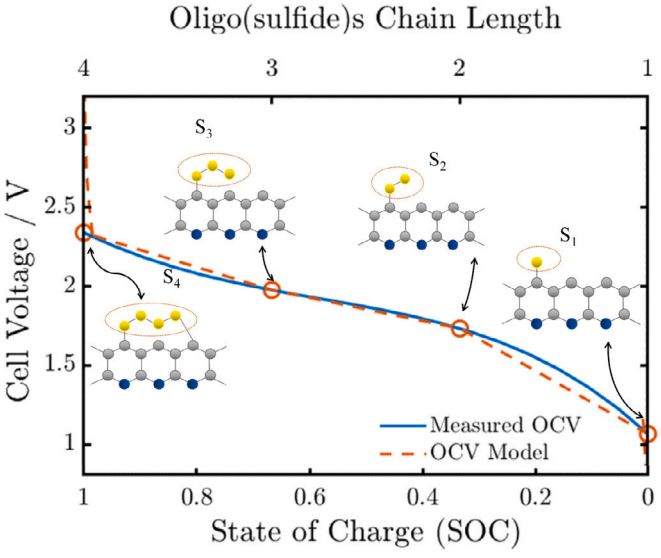

Fig. 3. Open Circuit Voltage (OCV) of Li-SPAN battery determined from experiment. The dashed line indicates the corresponding OCV $U_{S_x}^{\text{eq},0}$ used in our model according to Eq. (7).

In our model we employ an expression for the rate r_{S_x} of electrochemical reactions according to [59,60]

$$r_{S_x} = k^0_{f,S_x}\, a_{\text{ed.}}^{1-\alpha_{S_x}}\, a_{\text{prod.}}^{\alpha_{S_x}} \left(e^{-\frac{\alpha_{S_x}}{RT}\Delta\bar{\mu}_{S_x}} - e^{\frac{1-\alpha_{S_x}}{RT}\Delta\bar{\mu}_{S_x}} \right), \tag{4}$$

where R, T, k^0_{f,S_x}, and α_{S_x} are the ideal gas constant, temperature, frequency factor, and symmetry factor of the reaction. The terms $a_{\text{ed.}}$ and $a_{\text{prod.}}$. represent the products of the activities of the active species in the electrolyte according to

$$a_{\text{ed.}} = \prod_{\text{i=ed}} a_i^{|\upsilon_{i,S_x}|} \text{ and } a_{\text{prod.}} = \prod_{\text{prod}} a_i^{|\upsilon_{i,S_x}|}\ , \tag{5}$$

where υ_{i,S_x} are the stoichiometric coefficients of the reaction (1), (2), and (3). In our model we treat the liquid electrolyte as an ideal solution and the activity is given by $a_i = \bar{c}_i$, $\bar{c}_i = c_i/c_i^{\text{ref}}$ assuming $\gamma_i = 1$. The reference concentration of species i is chosen as the initial condition. Note, in the case of S^{2-} this corresponds to the solubility product of Li_2S. The activity of the SPAN species follows the general form $a_{S_i} = \gamma_{S_i}\bar{c}_{S_i}$. The reference concentration is given by the concentration of PAN-S_4-PAN chains and PAN-S_xLi, respectively (see Fig. 3).

The electrochemical potential difference of this electrochemical reaction (Eq. (4)) [41] can be generally written as

$$\Delta\bar{\mu}_{S_x} = nF(\phi_{\text{elode}} - \phi_{\text{elyte}} - U^{\text{eq}}_{S_x}). \tag{6}$$

where n is the number of moles of electrons transferred in the reaction. Following the reactions given in Eqs. (1)–(3), we use the value of $n = 1$ $U^{\text{eq}}_{S_x}$ is the equilibrium potential of the SPAN reaction according to

$$U^{\text{eq}}_{S_x} = \frac{1}{nF}\left(\Delta\mu^0_{S_x} + RT\ln\gamma_{S_x}(\bar{c}_{S_x}) + RT\ln\left(\frac{\bar{c}_{\text{ed}}}{\bar{c}_{\text{prod}}}\right)\right). \tag{7}$$

Based on the measured open circuit voltage we assume a linear dependence of the second term on the right hand side of Eq. (7) on the local reaction coordinate ζ_{S_x} of the three SPAN reactions implemented in our model. We can rewrite Eq. (7) according to

$$U_{S_x}^{\text{eq, ref}} = \frac{\Delta\mu_{S_x}^0}{nF} + \frac{RT}{nF}\ln\gamma_{S_x}\left(\zeta_{S_x}\right) = U_{S_x}^{\text{eq},0} - b_{S_x}\cdot\zeta_{S_x}\,, \tag{8}$$

where ζ_{S_x} is defined as $\zeta_{S_x} = 1 - \bar{c}_{S_x}$. Note, that γ_{S_x} is the ratio of the products of activity coefficients defined in Eq. (5). The resulting coefficients $U_{S_x}^{\text{eq},0}$ and b_{S_x} are extracted by the corresponding OCV measurements in Table 3.

2.3.3. Li_2S formation

In our model we take into account the formation of Li_2S during discharge. The precipitation reaction is written as

$$2\,Li^+ + S^{2-} \rightleftharpoons Li_2S^{(S)}\,. \tag{9}$$

Using the same formalism to describe the reaction rate

$$r_{Li_2S} = k_{f,Li_2S}^0\left(a_{Li^+}a_{S^{2-}}\right)^{\alpha_{Li_2S}}\left(e^{-\frac{\alpha_{Li_2S}}{RT}\Delta\bar{\mu}_{Li_2S}} - e^{\frac{1-\alpha_{Li_2S}}{RT}\Delta\bar{\mu}_{Li_2S}}\right). \tag{10}$$

The chemical potential difference of the reaction Eq. (9)given by

$$\Delta\bar{\mu}_{Li_2S} = \bar{\mu}_{Li_2S} - 2\bar{\mu}_{Li^+} - \bar{\mu}_{S^{2-}}\,, \tag{11}$$

$$= \mu_{Li_2S}^0 - 2\mu_{Li+}^0 - \mu_{S^{2-}}^0 - RT\ln(a_{Li^+}^2 a_{S^{2-}})\,. \tag{12}$$

This expression can be reformulated making use of the solubility product $K_{Li_2S}^{sp}$ resulting in

$$K_{Li_2S}^{sp} = \exp\left(\frac{\Delta\mu_{Li_2S}^0}{RT}\right), \tag{13}$$

$$\Delta\bar{\mu}_{Li_2S} = RT\ln K_{Li_2S}^{sp} - RT\ln(a_{Li^+}^2 a_{S^{2-}})\,. \tag{14}$$

In our model we consider the precipitation of $Li_2S^{(S)}$ on cathode surfaces only.

2.4. Parameterization

In this section we summarize the parameters defining geometry, electrochemistry, transport properties, and thermodynamics of the Li-SPAN cell.

2.4.1. Geometric parameters

The geometric parameters of the simulation domain describing the experimental setup are summarized in Table 1. Relevant geometric parameters are the thickness of the separator and the electrode, the volume fractions of SPAN, conductive additive, binder (CB), and Li_2S, as well as the corresponding surface areas between them. An important geometric parameter of the porous electrodes and the separator is also the tortuosity of the electrodes. Note that in the case of the Whatman glass fiber separator, the thickness and porosity of the separator when compressed in the Swagelok cell must be considered. Several methods have been used to estimate the porosity of this separator [61–63]. For our model, we use the thickness and porosity of the separator reported by Raccichini et al. [64]. In our framework, we use the Bruggeman correlation to compute the effective transport parameters. For the cathode and separator, we assign values of 1.5 and 1, respectively. Additionally, in Section 4.5, we evaluate the impact of the cathode Bruggeman coefficient on the performance of the battery.

2.4.2. Transport

Electrolyte. In this paper we simulate Li-SPAN batteries using a standard carbonate based electrolyte. The concentration dependent diffusion coefficients of Li^+ (D_{Li^+}) and PF_6^- ($D_{PF_6^-}$) ions are calculated based on the parameters measured by Lundgren et al. [65]. The diffusion coefficient of S^{2-} is assumed to be concentration independent and we choose a value in the order of magnitude reported by Ghaznavi et al. [36]. In Table 2 we report values at the initial conditions.

Table 1
Geometrical parameters defining the simulation domain. The values of concentrations, volume fractions, and surface areas are initial values and change during the simulations.

Cathode	
Thickness L_{cat}	100 µm
Specific surface area a_{SPAN}^v	$1{\cdot}10^7$ m^{-1}
Phases	
Carbon & Binder (CB)	
Volume fraction ε_{CB}	0.032
CB density ρ_{CB}	1810 kg/m^3
SPAN	
Volume fraction ε_{SPAN}	0.0945
SPAN density ρ_{SPAN}	1440 kg/m^3
Li_2S	
Volume fraction ε_{Li_2S}	$1\cdot10^{-5}$
Li_2S density ρ_{Li_2S}	1659 kg/m^3
Surface exponent ξ	1.5
Porosity φ_{cat}	0.87
Separator	
Thickness L_{sep}	618 µm (2 × 309 µm)
Phases	
Whatman Glass Fiber	
Volume fraction ε_{sep}	0.11
separator density ρ_{sep}	254 kg/m^3
Porosity φ_{sep}	0.89
Anode	
Thickness L_{an}	1 mm (Alfa Aesar)
Phases	
Li metal	
Volume fraction ε_{an}	1
Li density ρ_{Li}	530 kg/m^3

Table 2
Transport parameters of species in electrolyte and solid phases.

Parameter	Value	Meaning	Ref.
Electrolyte			
D_{LiPF_6}	$2.52\cdot10^{-10}$ m^2/s	Li^+, PF_6^- diffusion coefficient	[65]
$D_{S^{2-}}$	$4.7\cdot10^{-10}$ m^2/s	S^{2-} diffusion coefficient	[36]
t_{Li^+}	0.1625	Li^+ transference number	[65]
$\kappa^0_{LiPF_6}$	0.796 S/m	Electrolyte conductivity	[65]
$\left(1+\frac{\partial\ln f_c}{\partial\ln c_e}\right)$	1.6	Thermodynamic factor	[65]
$c^0_{Li^+}$	1000.02 mol/m^3	Li^+ initial concentration	[a]
$c^0_{PF_6^-}$	1000 mol/m^3	PF_6^- initial concentration	[a]
$c^0_{S^{2-}}$	0.01 mol/m^3	S^{2-} initial concentration	[a]
Solid			
κ_{SPAN}	1 S/m	Electronic conductivity	[a]
β_{cat}	1.5	Cathode Bruggeman coefficient	[a]
β_{sep}	1	Separator Bruggeman coefficient	[a]
c_{DL}	0.1 F/m^2	Double layer capacity	[a]
Z_{CC}	0.025 Ωm^2	Cathode contact resistance	[a]

[a] Assumed parameter.

Solid phases. In the SPAN electrode, we primarily consider the transport of electrons using an effective electronic conductivity of the material. Due to the relatively high conductive additive content, the conductive pathways are mainly through the conductive carbon, resulting in a high effective conductivity of 1 S/m. In our measurements we see a high potential drop at high currents which we mainly attribute to a contact resistance (Z_{CC}) between the current collector and the positive electrode layer. We find the best agreement with the experimental data at 0.035 Ωm^2.

2.4.3. Kinetic parameters

The kinetic and thermodynamic parameters of chemical and electrochemical reactions are calibrated against experimental data or taken

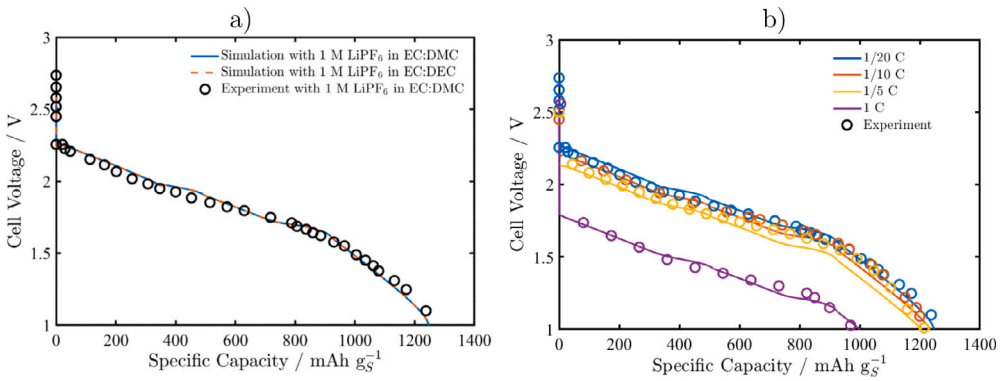

Fig. 4. Results of Galvanostatic Simulations. (a) Discharge curves of pseudo-OCV simulations (1/20 C = 0.05 mA/cm^2) using transport parameters of 1 $LiPF_6$ in EC:DEC and 1 $LiPF_6$ in EC:DMC solvent in simulation. (b) Discharge curves at various C-rates.

from the literature. A summary of the parameters can be found in Table 3.

SPAN kinetics. The kinetic and thermodynamic parameters of the SPAN reactions are the open circuit voltage (OCV) $U^{eq,0}_{S_x}$, pre-exponential factor k^0_{f,S_x}, and the symmetry factor ($\alpha = 0.5$). In this study we determine a quasi-OCV as a function of the SOC by measuring the discharge curve at C/20 rate. Details of the experimental setup are described in the following paragraph. The pre-exponential factor was determined by fitting discharge curves at different C-rates. In general, we found a relatively low sensitivity to this parameter in our simulations (Figure S1). Detailed investigations of SPAN kinetics are planned for future work.

Li_2S precipitation and dissolution. In our simulations we model the precipitation of solid Li_2S in the cell. A decisive parameter is the solubility product. The solubility of polysulfides was found to be lower in carbonates than in ether-based solvents. Therefore, we use a solubility product of $K^{sp}_{Li_2S} = 10$. Other kinetic parameters are taken from our previous publications [41,43].

Li metal kinetics. Parameters for Li plating and stripping are taken from our previous work [41,43] and are used here without modification.

2.5. Simulation methodology

The model in this work was implemented in MATLAB and solved using ode15s. The system of partial differential equations was discretized using a finite volume scheme. For all simulations in this work, both cathode and separator were discretized using 20 and 10 discretization elements, respectively. The higher spatial discretization for cathode was chosen to ensure the accuracy of the simulation results. The simulation time of a galvanostatic discharge was in the order of a few minutes depending on the operation conditions. The higher spatial discretization for cathode was chosen to ensure the accuracy of the simulation results.

3. Experiments

The details of the electrode preparation, cell assembly, and electrochemical characterization of Li-SPAN cells are explained in this section.

3.1. SPAN cathode

The PAN material (Mn = 36,500 g/mol) was purchased from Merck and stored at room temperature in an Ar-filled glove box. Active material SPAN inside the positive electrode was prepared via a two-step reaction. First, circa 1 g of PAN powder was mixed homogeneously with excess (15 g) sulfur powder inside a high-temperature resistant quartz glass tube and was heated up to 150 °C under Ar. The tube was then cooled to room temperature after all the sulfur was completely molten and put inside a furnace. The oven temperature was set initially at 150 °C and was held for 30 min. The temperature was increased gradually to 550 °C over 3 h and then held for 5 h. Then the furnace was cooled down overnight and the tube was removed. To remove excess sulfur, the SPAN was extracted in a Soxhlet apparatus using hot toluene for 2 days until no further sulfur could be extracted. The obtained SPAN compound was further dried in vacuum overnight and then manually ground using a mortar and a pestle to reduce the particle size of the SPAN particles. The SPAN particles were sieved by a 63 µm sieve to ensure a homogeneous particle size distribution. Elemental analysis of SPAN showed the following elemental composition: C, 44.08%; H, 1.048%; N, 13.66%; S, 38.32%.

The positive electrode was prepared with a weight ratio of SPAN: Carbon Black:Binder of 70:15:15 with poly(vinylidene difluoride) (PVDF) as binder material. The weight ratio of N-methyl-2-pyrrolidone (NMP): SPAN was set to 10:1. The dispersion of SPAN, conductive material, the binder and NMP were mixed at 20,000 rpm for 6 min. Next, the slurry was coated on a graphite foil and dried on a vacuum plate at 60 °C under air suction for several hours. As the coating was almost dry, it was placed in an oven at 60 °C to continue the drying process. Round chips with 12 mm in diameter were punched out. The sulfur content of our SPAN material was 43.6-wt-% resulting in a theoretical specific capacity of 728.12 mAh/g_{SPAN}. To avoid breakage of S-C bonds we limited the lower cut-off voltage to 1 V which reduces the maximum practical capacity. We assumed that the average sulfur chain length was around 4. In this case the usable practical capacity is 75% of the theoretical capacity (546.09 mAh/g_{SPAN}). The average sulfur content was 0.6 mg/cm^2 per cathode (SPAN loading of 2.91 mg/cm^2), corresponding to an areal capacity of 0.6 mAh/cm^2.

3.2. Cell assembly and test procedure

The battery cells were assembled in a glove box under argon atmosphere. Cycling tests and measurements of discharge–charge profiles were made on Swagelok type cells comprising an SPAN cathode (12 mm diameter), two Whatman glass fiber separators, and a lithium metal anode (12 mm diameter).

The quasi-OCV measurements were carried out using 1M $LiPF_6$ in EC:DMC solvent (1 : 1) at a C/20 rate. All rate tests were performed using 1M $LiPF_6$ in EC:DEC (1 : 1) as solvent. The discharging and charging tests were performed at constant currents of 0.05 mA/cm^2, 0.1 mA/cm^2, 0.2 mA/cm^2, and 1 mA/cm^2. The cells were cycled between 1.0 – 3.0 V to avoid decomposition of the electrolyte at higher voltage [66]. The cycling data was recorded on a BasyTec XCTS-LAB system.

Table 3
Kinetic parameters for electrochemical and chemical reactions.

Parameter	Value	Meaning	Ref.
Electrochemical reactions			
SPAN cathode			
$1/2\ \mathbf{PAN\text{-}S_4\text{-}PAN} + \mathbf{Li^+} + e^- \rightleftharpoons 1/2\ \mathbf{PAN\text{-}S_3Li} + 1/2\ \mathbf{PAN\text{-}S_1Li}$			
k^0_{f,S_4}	$1 \cdot 10^{-2}$ mol/m^2 s	Frequency factor of reaction	b
α	0.5	Symmetry factor of transition state	b
$U^{eq,0}_{S_4}$	2.2 V	Parameters for the calculation of the SPAN OCP	b
b_{S_4}	0.3 V		b
$1/2\ \mathbf{PAN\text{-}S_3Li} + e^- \rightleftharpoons 1/2\ \mathbf{PAN\text{-}S_2Li} + 1/2\ \mathbf{S^{2-}}$			
k^0_{f,S_3}	$1 \cdot 10^{-2}$ mol/m^2 s	Frequency factor of reaction	b
α	0.5	Symmetry factor of transition state	b
$U^{eq,0}_{S_3}$	1.9 V	Parameters for the calculation of the SPAN OCP	b
b_{S_3}	0.28 V		b
$1/2\ \mathbf{PAN\text{-}S_2Li} + e^- \rightleftharpoons 1/2\ \mathbf{PAN\text{-}SLi} + 1/2\ \mathbf{S^{2-}}$			
k^0_{f,S_2}	$1 \cdot 10^{-4}$ mol/m^2 s	Frequency factor of reaction	b
α	0.5	Symmetry factor of transition state	b
$U^{eq,0}_{S_2}$	1.66 V	Parameters for the calculation of the SPAN OCP	b
b_{S_2}	0.62 V		b
$c^0_{S_4}$	598 mol/m^3	PAN-S_4 initial concentration	b
$c^0_{S_3}$	$1{\cdot}10^{-5}$ mol/m^3	PAN-S_3Li initial concentration	b
$c^0_{S_2}$	$1{\cdot}10^{-5}$ mol/m^3	PAN-S_2Li initial concentration	b
$c^0_{S_1}$	$1{\cdot}10^{-5}$ mol/m^3	PAN-SLi initial concentration	b
$c_{S_4,ref}$	598 mol/m^3	PAN-S_4 reference concentration	b
$c_{S_3,ref}$	598 mol/m^3	PAN-S_3Li reference concentration	b
$c_{S_2,ref}$	598 mol/m^3	PAN-S_2Li reference concentration	b
$c_{S_1,ref}$	1196 mol/m^3	PAN-SLi reference concentration	b
Li anode			
$\mathbf{Li^+} + e^- \rightleftharpoons \mathbf{Li}$			
$k^0_{f,Li}$	3.94 mol/m^2 s	Frequency factor of reaction	[43]
α	0.5	Symmetry factor of transition state	[43]
U^0_{eq}	0	OCP at reference condition	[43]
Chemical reaction			
$2\mathbf{Li^+} + \mathbf{S^{2-}} \rightleftharpoons \mathbf{Li_2S}$			
$K^{sp}_{Li_2S}$	$1 \cdot 10$	Solubility	a
$k^0_{Li_2S}$	$2 \cdot 10^2$ mol/m^2 s	Growth factor	a

[a] Assumed parameter.
[b] Fit to experimental data.

4. Results and discussion

In this section, the simulation results of the Li-SPAN cell model are presented. The novel model is used to study the electrochemical properties of Li-SPAN batteries and the relation to the design parameters relevant for upscaling and cell optimization.

4.1. Model validation

In Section 2.4 we provide a description of the parameterization procedure of our model. Parameters have been adjusted on the basis of dedicated measurements as well as data published in the literature. In this section, we will validate our model by comparing the simulations to the rate tests measured on the Li-SPAN cells shown in Fig. 4.

First, we compare our simulation results to the measurements at C/20 rate serving as input for the SPAN equilibrium potentials $U^{eq,\ ref}_{S_x}$. Note that these quasi-OCV measurements were made in Li-SPAN cells using EC:DMC electrolyte. Simulations in the main part of the manuscript are all done using electrolyte parameters for 1 M $LiPF_6$ in EC:DEC which is the electrolyte system used in subsequent rate tests. Still, we can report a good agreement between measurements and simulations at the C/20 rate. Simulations comparing the predictions of the C/20 charge and discharge curves using transport parameters of 1 M $LiPF_6$ in EC:DMC [67] and 1 M $LiPF_6$ in EC:DEC [65] are shown in Fig. 4a.

The simulated discharge curves at varying C-rate (Fig. 4b) of our newly developed Li-SPAN model are in good agreement with the experimental data. At moderate C-rates, the cell voltage of both measurements and simulations show negligible overpotentials resulting in very similar discharge curves. However, at a high 1 C rate, we observe a significant increase in overpotential.

In our model, we assume that a contact resistance between the SPAN cathode and current collector causes this significant loss in performance. However, the kinetics of the electrochemical reactions or transport in the electrolyte can cause similar performance losses. We will analyze the different contributions in the following sections.

4.2. Discharge mechanism of SPAN

The cell simulations allow us to study the kinetics and discharge mechanism of the SPAN material. The measured discharge curve does not exhibit the typical two-stage profile of conventional Li–S batteries, which confirms the absence of dissolved polysulfides in the electrolyte. Instead, we observe a rather continuous decrease of the cell voltage during discharge. In our model we link this to the reduction and extraction of S^{2-} from the oligo(sulfide) chain followed by the precipitation of solid Li_2S. Therefore, only S^{2-} can be found in the electrolyte. Concentrations are generally low and determined by the solubility in the carbonate based electrolyte system.

Fig. 5a shows the evolution of sulfur chains with different length during discharge at 1/10 C rate (0.1 mA cm^{-2}). At the beginning of

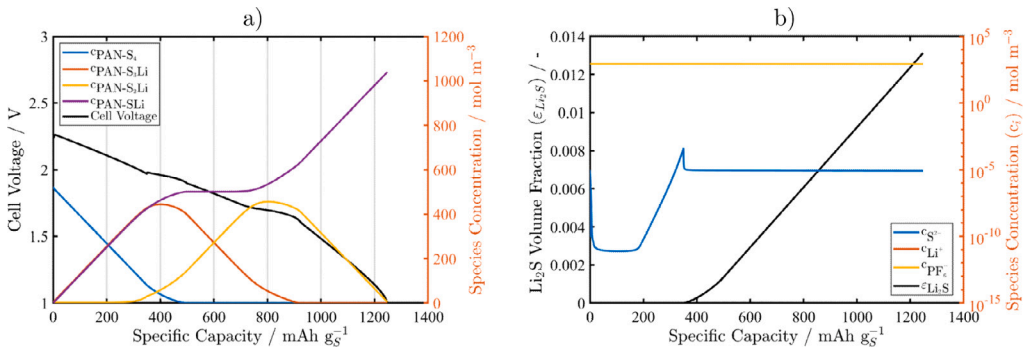

Fig. 5. Galvanostatic discharge simulation at 1/10 C (0.1 mA cm^{-2}). (a) Cell voltage (black line, left axis) and corresponding PAN-S$_x$ concentrations (right axis) as function of specific capacity, (b) Li$_2$S volume fraction ϵ_{Li_2S} (left axis) in the cathode and average species (Li$^+$, PF_6^-, S^{2-}) concentration (right axis) in the cathode.

discharge, most of the oligo(sulfide) chains have a length of 4 sulfur atoms with each end connected to the PAN matrix. During discharge, the concentration of PAN-S$_4$ oligo(sulfide) chains c_{S_4} is reduced while shorter oligo(sulfide) chains (PAN-S$_3$Li and PAN-SLi) are formed. Note that during operation at practical rates, a mixture of oligo(sulfide) chains of different length coexist, resulting in a mixed potential due to the different SPAN reduction reactions. This is indicated by the continuous increase of c_{S_3} and c_S before all PAN-S$_4$ chains are reduced. As the discharge continues, the concentration of PAN-S$_3$Li chains decreases, followed by an increase of shorter (PAN-S$_2$Li, PAN-SLi) chains. At the end of the discharge, almost all available sulfur atoms have been extracted, leaving only chains with one sulfur atom on the polymer backbone (PAN-SLi). Note that this is the minimum we assume and that is required for stable cycling. Therefore, not all possible oligo(sulfide)s are reduced during discharge, resulting in a reduced capacity, which is also observed in the experiments.

Fig. 5b shows the evolution of Li$_2$S volume fraction and the average concentration of dissolved species (Li$^+$,PF_6^-,S^{2-}) in the SPAN cathode during discharge. In the first discharge phase, which mainly involves the reduction of PAN-S$_4$, the Li$_2$S volume fraction is negligible. In the second phase we model the formation of PAN-S$_2$Li which also causes an increase of S^{2-} concentration in the electrolyte. Due to the low solubility product of Li$_2$S, the S^{2-} concentration rapidly reaches the solubility limit of around 10^{-5} mol/l. At this point the Li$_2$S volume fraction begins to grow and we observe a linear increase in the second and third discharge phases.

Our simulation results suggest that the S^{2-} concentration in the electrolyte varies within a very small range during discharge. Therefore, the concentration of Li$^+$ and PF_6^- is close to the initial value of 1000 mol/m^3 to maintain electroneutrality. The effect of Li$_2$S solubility and kinetics will be discussed in Section 4.6. In our model we do not take into account side reactions of the polysulfides at the anode due to the very low polysulfide solubility in the carbonate based electrolyte. However, incorporation of the polysulfide shuttle is straight forward and has been investigated for conventional Me-S batteries [6,58].

4.3. Effect of SPAN kinetics

An interesting feature in the rate test are the large overpotentials observed at high currents. To understand the limiting factors for battery performance, we vary the exchange current density of the SPAN electrochemical reactions. Fig. 6a shows discharge curves for different values of the kinetic prefactor $k^0_{f_{S_x}}$. In order to isolate the effect of SPAN kinetics, we set the contact resistance Z_{CC} equal to zero. During parameterization $k^0_{f_{S_x}}$ was adjusted to 10^{-4} to reproduce the discharge curve at 1/10 C rate. Fig. 6a shows that there is quite a discrepancy between our simulation result and the experiment for a current of 1 C. However, this discrepancy cannot be resolved even by reducing the kinetic prefactor by orders of magnitude. The cell voltage consistently decreases with decreasing prefactor. However, the prefactor reduces the cell voltage for both 1/10 C and 1 C rate. Therefore, we conclude that the observed overpotential at high C rate is not due to SPAN kinetics.

4.4. Effect of contact resistance

In the previous paragraph we studied the effect of SPAN kinetics. Although sluggish kinetics generally result in significant overpotentials, the resulting charge transfer resistance is contradictory to the good rate performance of SPAN material reported in the literature. Other relevant parameters are the electrical contact or, more general, the electrical conductivity of the SPAN cathode. Due to the high amount of conductive additives, the latter property is unlikely to affect the battery performance. Therefore, we focus on the influence of contact resistance Z_{CC} on battery performance. Fig. 6b shows discharge simulations with varying contact resistance between SPAN and the current collector. We observe that for simulations with low C rate, the cell voltage does not deviate much despite an increasing contact resistance Z_{CC}. However, for simulations at higher C rate, the overpotential increases significantly as we increase Z_{CC}, providing a good agreement with the experimental data at $Z_{CC} = 0.025$. On the basis of these results, we conclude that the significant overpotential of the SPAN cells at higher C rate is a result of the electrical resistance between SPAN cathode and the cathode current collector. This might be due to the mechanical properties of the SPAN material that allows only moderate compression or calendering of the material.

4.5. Effect of ionic resistance

The electrodes investigated in this work have a SPAN content of only 10 vol-% (Table 1) which corresponds to a sulfur loading of 0.6 mg/cm^2 (0.8 mAh/cm^2). The electrode tortuosity or its corresponding Bruggeman coefficient β_{elyte}, affect the ion transport in the porous SPAN cathode. Since the SPAN electrode is highly porous, the reduction of effective transport parameters is not significant. Therefore, the effect on electrochemical processes is minor. Figure S2 shows the simulated cell voltage at low 1/10 C and high 1 C current rate for different values of the positive electrode tortuosity [19,68]. Even for high tortuosity values, no effect on cell voltage can be observed, which suggests that ion transport in the electrolyte is not limiting in the lab scale electrodes.

4.6. Effect of Li_2S solubility and kinetics

The electrochemical reactions of SPAN during discharge affect the concentration of S^{2-} in the electrolyte. The maximum concentration of S^{2-} is governed by the solubility of Li$_2$S in the electrolyte. Above the solubility limit we model the formation of the solid discharge product Li$_2$S. The decisive properties and parameters of this process are the

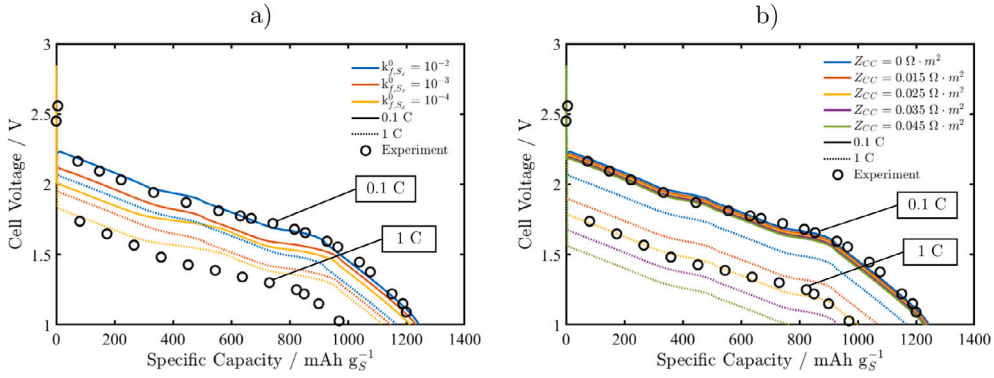

Fig. 6. (a) Discharge simulation for 1/10 C and 1 C (1/10 C = 0.1 mA cm^{2-}) with varying SPAN kinetics (Z_{CC} = 0). (b) Discharge simulation for 1/10 C and 1 C (1/10 C = 0.1 mA cm^{2-}) with varying contact resistance (Z_{CC}).

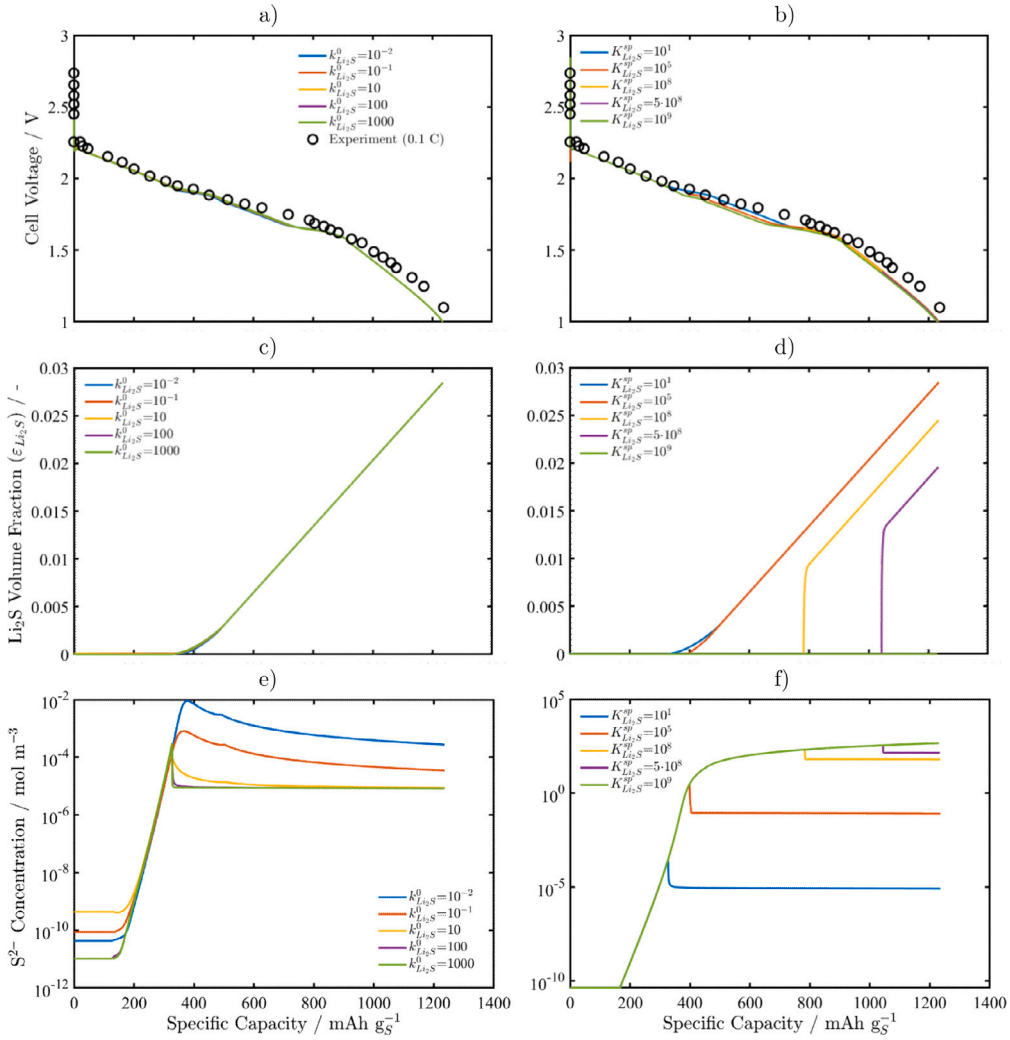

Fig. 7. Left column: Galvanostatic discharge simulation (1/10 C) with varying precipitation kinetics $k^0_{Li_2S}$. (a) cell voltage, (c) Li$_2$S volume fraction, (e) average S^{2-} concentration in the electrolyte (cathode only). Right column: Galvanostatic discharge simulation (1/10 C) with varying solubility product ($K^{sp}_{Li_2S}$: b) cell voltage, (d) Li$_2$S volume fraction, (f) average S^{2-} concentration in the electrolyte (cathode only).

solubility product $K^{sp}_{Li_2S}$ and kinetic factor $k^0_{Li_2S}$. In this paragraph we study the effect of these parameter operations. Fig. 7 gives an overview of the simulation study. The effect of Li_2S precipitation kinetics is depicted in the left column and the effect of Li_2S solubility is shown in the right column.

Li_2S kinetics. - The left column of Fig. 7 depicts galvanostatic discharge simulations with varying Li_2S precipitation kinetics. During discharge, Li_2S precipitates in the electrolyte and consumes S^{2-}, which is extracted from oligo(sulfide) chains on the PAN material. Based on our simulation study, the precipitation kinetics have no significant effect on the cell voltage. Fig. 7c shows that for all precipitation rates, the formation of Li_2S is not significantly affected. Yet, with faster precipitation rates ($>10^{-1}$) the S^{2-} concentration is close to the solubility limit of 10^{-5} mol/m^3 given by the Li_2S solubility product of $K^{sp}_{Li_2S} = 10$.

In the present study, we do not incorporate charging mechanism in our model. Nevertheless, it is worth acknowledging that these aspects will be significant for our future research, as the kinetics of Li_2S dissolution may potentially limit the charging rate of the Li-SPAN cells. If the dissolution rate is slower than the SPAN conversion rate, the supply of S^{2-} limits the capacity of the cell.

Li_2S solubility. - The right column of Fig. 7 shows galvanostatic discharge simulations with varying Li_2S solubility in the electrolyte using a constant kinetic factor $k^0_{Li_2S}$ of $2 \cdot 10^2$. Fig. 7b shows discharge curves for different values of the solubility product. In general, the solubility has no significant effect on the cell voltage, with the notable exception of the region between 400–700 mAh/g_S where a small overpotential is observed. The overpotential in the cell voltage is related to the concentration of S^{2-} anions in the electrolyte (Fig. 7f) as given by Eq. (7). Note that initially the concentration of lithium ions is given by the salt concentration of 1000 mol/m^3. However, during operation the local concentration of lithium ions may vary, affecting the maximum local S^{2-} concentration.

In an electrolyte with a low solubility($K^{sp}_{Li_2S} < 10^5$), the S^{2-} concentration rapidly approaches the solubility limit. As a consequence Li_2S precipitates almost instantaneously (Fig. 7d) and grows linearly during discharge. At high solubility products ($K^{sp}_{Li_2S} > 10^5$) the concentration of S^{2-} needs considerably longer to approach the solubility limit. Consequently, the formation of Li_2S is delayed. However, the initial increase in Li_2S volume fraction is faster for high solubility products due to faster kinetics favored by higher concentrations in the electrolyte. After the nucleation phase, the S^{2-} concentration in the electrolyte decreases rapidly due to the growth of Li_2S before reaching a steady-state, resulting in a linear increase in the Li_2S volume fraction.

Finally, if the solubility product is sufficiently large no Li_2S precipitation is observed, resulting in a continuous increase of S^{2-} concentration in the electrolyte. Note that the Li_2S precipitate reduces both the active surface and the pore volume for electrolyte transport. However, in the current cell design the sulfur loading is not sufficient to have a significant impact on battery performance. We will revisit this aspect in Section 4.7.

4.7. Perspective on Li-SPAN development

The purpose of our work is to provide theoretical tools for the development and commercialization of Li-SPAN batteries. Hence, we aim to bridge the gap between cells that are developed in research and academia to cell designs targeting at commercialization. One of the most important aspects for the commercialization of Li–S batteries is the energy density of the cells.

To provide predictions of the influence of electrode and cell design on specific energy we first define electrode and cell parameters targeting at cells with high energy density. We use an optimized electrode formulation of 90 wt-% SPAN and 10 wt-% carbon black and binder and fix the thickness of the electrode and separator to 100 µm and 20 µm, respectively. Moreover, we assume a balancing factor of negative to positive electrode capacity of 1.2. Another decisive factor in LiS development is the electrolyte content. The target of cell development is a low electrolyte contents of 1.5 g/Ah [69] which is similar to the values reported for LIBs. Note, that such lean electrolyte conditions might be detrimental for the cycle life [70] of the lithium metal cells. Therefore, we provide estimates of the theoretical capacity with a higher electrolyte content of 3 g/Ah. Additionally, we assume in all cases a minimum electrolyte content for full wetting of the available pore volume. In the LiS community it is common to relate the electrolyte content to the sulfur loading. 1.5 and 3 g/Ah correspond to approximately 2 and 4 ml/g_S, respectively. Details of the calculations are summarized in the supporting material.

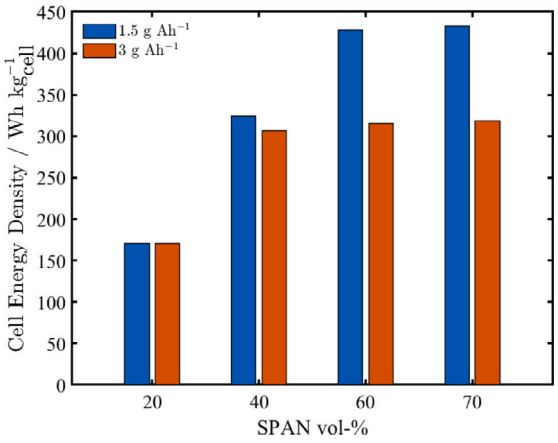

Fig. 8. Bar chart providing cell level of theoretical specific energy for a projected, optimized cell design (see Table S3 and S4) as function of electrode density, represented by the volume fraction of SPAN material. Blue and red color represent an electrolyte content of 1.5 and 3 g/Ah, respectively.

The theoretical specific energy as function of SPAN content is shown in Fig. 8. On the basis of these calculations, Li-SPAN cells are potentially able to achieve a very high specific energy close to 450 Wh/kg_{cell} on cell level. The electrolyte content has a significant effect on the theoretical specific energy. However, even with 3 g/Ah the projected cell designs allow for specific energy above 300 Wh/kg. The graph demonstrates that increasing the SPAN content generally increases the specific energy of the SPAN cell. However, along with SPAN content the electrode capacity and electrolyte content increase. For high SPAN contents the electrolyte significantly increases the mass of the cell, resulting in negligible improvements in specific energy despite high areal capacity (see Fig. 9). In particular, the calculations indicate that SPAN contents exceeding 60 vol-% provide no significant improvements in specific energy. Nevertheless, the calculations show that SPAN is a promising material for future application in the mobility sector.

Based on this assessment, we simulate discharge curves using the optimized electrode formulation and cell design described above. Note, that the electrolyte-to-sulfur (E/S) ratio is a critical factor for conventional Li–S batteries when going from coin cells to pouch cells. The amount of liquid electrolyte influences the dissolution of intermediate polysulfide species. In Li-SPAN cells with carbonate-based electrolytes the solubility of Li_2S is generally low. Therefore, effects on SPAN discharge is minor. Still, limited supply of electrolyte has a negative impact on cycle life as discussed in previous paragraphs.

The left column of Fig. 10 shows results of 1 C discharge simulations for SPAN cathodes with varying SPAN volume fraction (ε_{SPAN}). In all cases the Bruggeman coefficient, which represents the tortuosity of the electrode, is set to 1.5. This corresponds to the value of an ideal packing of spherical particles [71]. The corresponding discharge curves are shown in Fig. 10 (a). For SPAN contents between 20 and 60 vol-%,

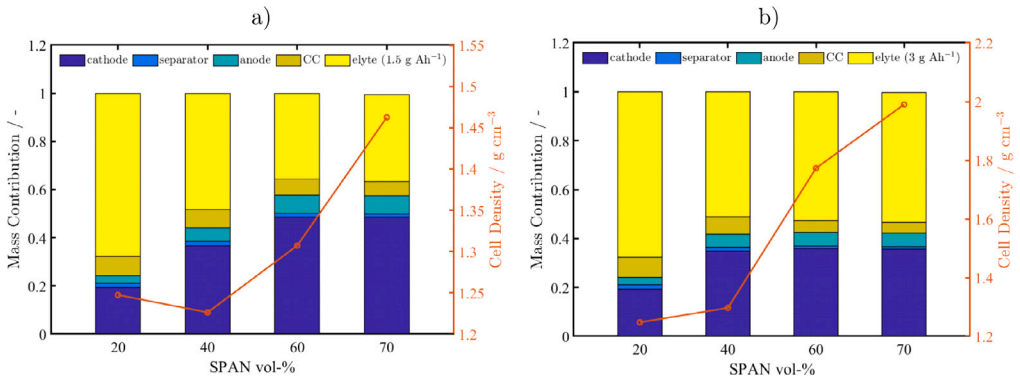

Fig. 9. Bar chart providing theoretical mass contribution and total cell mass density for a projected, optimized cell design represented by the volume fraction of SPAN material for electrolyte content of (a) 1.5 and (b) 3 g/Ah, respectively.

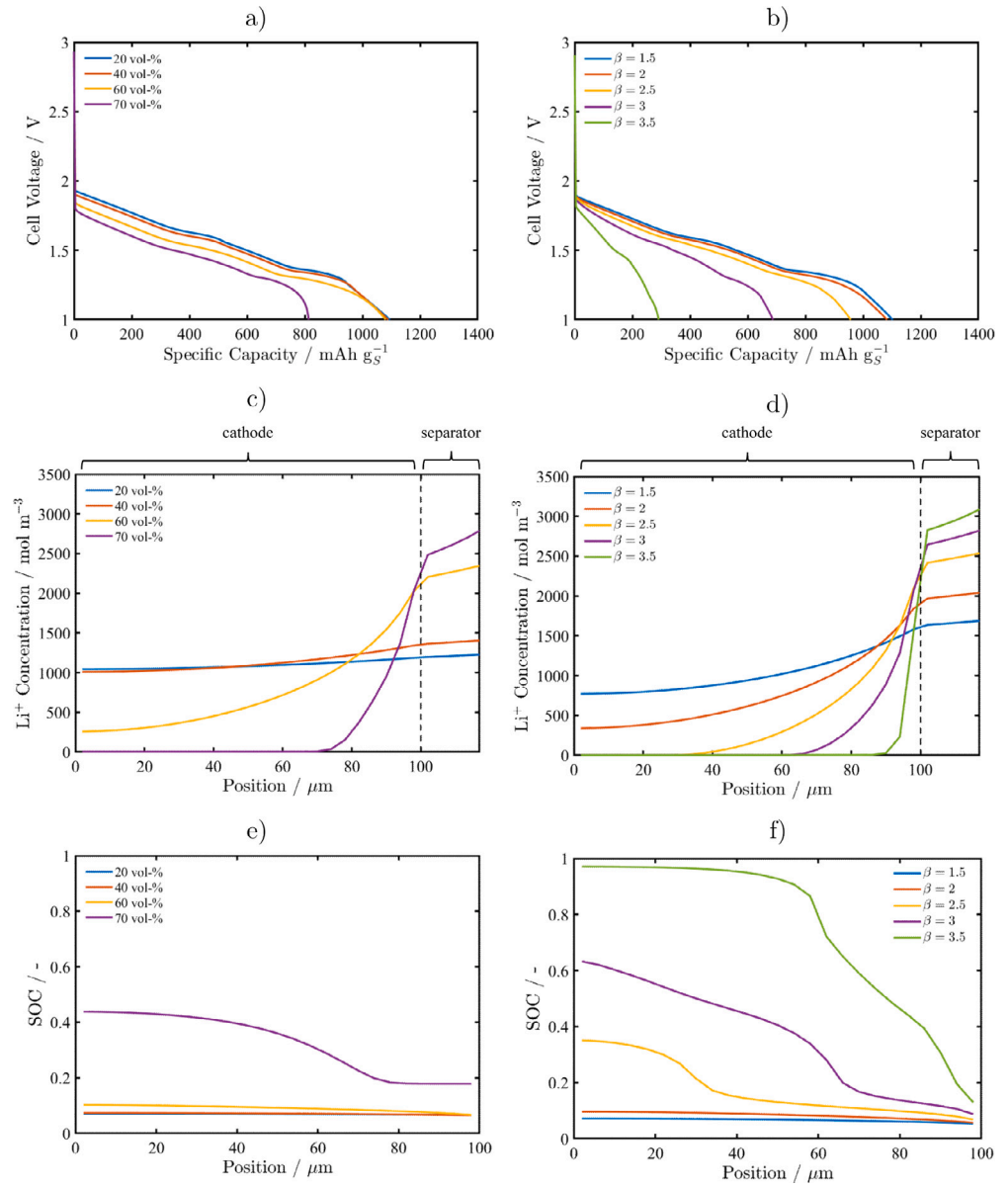

Fig. 10. Simulation results for the projected high specific energy cell design. All graphs show results of a 1 C discharge process. The left column presents a variation in the SPAN content at a constant Bruggeman coefficient $\beta_{\text{elyte}} = 1.5$. The right column presents the effect of increasing electrode tortuosity at a constant electrode density given by the SPAN content of 60 vol-%. The first row shows (a), (b) discharge curves (c), (d) lithium ion concentration in the electrolyte from cathode current collector (0 µm) to lithium metal surface (120 µm) at the end of discharge (1 V) (e), (f) SPAN utilization in the cathode at the end of the discharge (1 V).

the effect on the discharge curves and discharge capacity is moderate. However, at 70 vol-% SPAN in the electrode, the discharge capacity drops to 800 mAh/g_s. Our simulations indicate that ion transport limits cell performance at high electrode densities. Fig. 10 (c) shows a significant drop in lithium concentration in the cathode at 70 vol-% SPAN at the end of the discharge. The significant gradient in the lithium ion concentration limits the utilization of SPAN near the current collector. Fig. 10 (e) shows the relative utilization of the SPAN material given by the remaining local capacity normalized to the initial capacity at the beginning of the discharge. The graph shows that SPAN utilization is generally lower at high electrode densities. In addition, the region near the CC is less utilized compared to the region near the separator with high lithium ion concentration.

The simulations indicate that volume fractions greater than 60 vol-% of SPAN are limited by ion transport in the electrolyte, even for a low electrode tortuosity (β_{elyte} = 1.5). Higher tortuosity values are typically reported in commercial electrodes [72,73]. The right column of Fig. 10 shows 1C discharge simulations of electrodes with 60 vol-% SPAN content and varying Bruggeman coefficient β_{elyte}. Fig. 10 (b) shows the corresponding discharge curves. Our simulations show that the electrode tortuosity is a sensitive parameter that significantly affects electrode performance. As the Bruggeman coefficient increases the capacity drops below 300 mAh/g_S. A limit for the presented cell design seems to be a Bruggeman coefficient of 2.5, which still results in a reasonable rate performance and should be a target for electrode development. Fig. 10 (d) shows the concentration distribution of lithium ions in the cathode. Above a Bruggeman value of 2.5, the lithium concentration in the cathode is close to zero at the current collector. Fig. 10 (f) shows that these conditions prevent full utilization of the SPAN capacity. Our simulations underscore the importance of a detailed structural analysis to determine the effective transport parameters of SPAN materials [19]. The structure or morphology of the cathode material plays a crucial role in the development of SPAN cells with high energy and power density. Similarly, Lebherz et al. [19] report a correlation between SPAN cathode tortuosity and its cycling stability. Thus, it is clear that increasing electrode density without proper electrode or cell design will not result in improved cell performance at relevant current densities.

5. Conclusions

SPAN is a promising cathode material for future Li–S batteries. Sulfur is bound to a polymer-derived backbone, which mitigates the polysulfide shuttle resulting in high coulombic efficiency and long cycle life. Moreover, our calculations indicate that specific energies of 500 Wh/kg can be achieved in optimized electrode and cell designs. Novel design tools are needed to avoid compromising the good rate performance reported on lab scale.

In this work we present for the first time a model of a Li-SPAN battery. We parameterize and validate the model against experimental data. The simulation results are in good agreement with measured discharge curves. On the basis of the simulations we investigate the discharge mechanism of the SPAN material and analyze the impact of different parameters and processes on cell behavior. Our simulation results suggest that the large overpotentials observed in the lab cells at high current densities are a result of a contact resistance between current collector and SPAN cathode. Moreover, we found that in the current electrode design transport in the electrolyte is not limiting cell performance. However, in cell designs targeting high energy density our simulations demonstrate that the morphology and microstructure of the SPAN cathode will be crucial to attain C-rates relevant for practical applications.

The newly developed SPAN model can be regarded as a design tool for Li-SPAN batteries. Thereby, it will be able to guide the development of new materials and the up-scaling of electrode and cell concepts.

CRediT authorship contribution statement

Esther Kezia Simanjuntak: Writing – original draft, Visualization, Software, Investigation, Conceptualization. **Timo Danner:** Writing – review & editing, Supervision, Project administration, Funding acquisition, Conceptualization. **Peiwen Wang:** Writing – review & editing, Investigation. **Michael R. Buchmeiser:** Writing – review & editing, Resources, Project administration, Funding acquisition. **Arnulf Latz:** Writing – review & editing, Supervision, Resources, Funding acquisition.

Declaration of competing interest

The authors declare that they have no known competing financial interests or personal relationships that could have appeared to influence the work reported in this paper.

Data availability

Data will be made available on request.

Acknowledgments

Financial support by the German Federal Ministry of Education and Research (BMBF) within the projects MagSiMal (project number 03XP0208) and SulForFlight (project number 03XP0491) is gratefully acknowledged. Additionally, this study contributes to the research performed at CELEST (Center for Electrochemical Energy Storage Ulm-Karlsruhe).

Appendix A. Supplementary data

Supplementary material related to this article can be found online at https://doi.org/10.1016/j.electacta.2024.144571.

References

[1] A. Manthiram, Y. F, S. Chung, C. Zu, Y. Su, Rechargeable lithium - sulfur batteries, Chem. Rev. 114 (23) (2014) 11751–11787, http://dx.doi.org/10.1021/cr500062v.

[2] L.J.H., J.-M.T. Peter, G. Bruce, Stefan A. Freunberger, Li – O 2 and Li – S batteries with high energy storage, Nature Mater. 11 (January) (2012) 19–30, http://dx.doi.org/10.1038/NMAT3191.

[3] S. Dörfler, H. Althues, P. Härtel, T. Abendroth, B. Schumm, S. Kaskel, Challenges and key parameters of lithium-sulfur batteries on pouch cell level, Joule 4 (3) (2020) 539–554, http://dx.doi.org/10.1016/j.joule.2020.02.006.

[4] Z. Zhao-Karger, X. Zhao, D. Wang, T. Diemant, R.J. Behm, M. Fichtner, Performance improvement of magnesium sulfur batteries with modified non-nucleophilic electrolytes, Adv. Energy Mater. 5 (3) (2015) http://dx.doi.org/10.1002/aenm.201401155.

[5] Y.V. Mikhaylik, J.R. Akridge, Polysulfide shuttle study in the Li/S battery system, J. Electrochem. Soc. 151 (2004) 1969–1976, http://dx.doi.org/10.1149/1.1806394.

[6] R. Richter, J. Häcker, Z. Zhao-Karger, T. Danner, N. Wagner, M. Fichtner, K.A. Friedrich, A. Latz, Insights into self-discharge of Lithium- and Magnesium-Sulfur batteries, ACS Appl. Energy Mater. 3 (9) (2020) 8457–8474, http://dx.doi.org/10.1021/acsaem.0c01114.

[7] H.S. Kim, T.S. Arthur, G.D. Allred, J. Zajicek, J.G. Newman, A.E. Rodnyansky, A.G. Oliver, W.C. Boggess, J. Muldoon, Electrolyte with a sulphur cathode, Nature Commun. 2 (2011) 426–427, http://dx.doi.org/10.1038/ncomms1435.

[8] S. Xiong, K. Xie, Y. Diao, X. Hong, Characterization of the solid electrolyte interphase on lithium anode for preventing the shuttle mechanism in lithium e sulfur batteries, J. Power Sources 246 (2014) 840–845, http://dx.doi.org/10.1016/j.jpowsour.2013.08.041.

[9] B. Bresser, D, i.S. Passerin, Scrosati, Sulfur-based lithium secondary batteries – a review, Chem. Commun. 49 (90) (2013) 10545, http://dx.doi.org/10.1039/c3cc46131a.

[10] S.S. Zhang, Liquid electrolyte lithium / sulfur battery : Fundamental chemistry, problems, and solutions, J. Power Sources 231 (2013) 153–162, http://dx.doi.org/10.1016/j.jpowsour.2012.12.102.

[11] P. Wang, M.R. Buchmeiser, Rechargeable magnesium–sulfur battery technology: State of the art and key challenges, Adv. Funct. Mater. (2019) 1905248, http://dx.doi.org/10.1002/adfm.201905248.

[12] T. Gao, S. Hou, F. Wang, Z. Ma, X. Li, K. Xu, C. Wang, Reversible S0/MgSx Redox chemistry in a MgTFSI2/MgCl2/DME electrolyte for rechargeable Mg/S batteries, Angew. Chem. - Int. Ed. 56 (43) (2017) 13526–13530, http://dx.doi.org/10.1002/anie.201708241.

[13] S.Y. Ha, Y.W. Lee, S.W. Woo, B. Koo, J.S. Kim, J. Cho, K.T. Lee, N.S. Choi, Magnesium(II) bis(trifluoromethane sulfonyl) imide-based electrolytes with wide electrochemical windows for rechargeable magnesium batteries, ACS Appl. Mater. Interfaces 6 (6) (2014) 4063–4073, http://dx.doi.org/10.1021/am405619v.

[14] X. Ji, K.T. Lee, L.F. Nazar, A highly ordered nanostructured carbon-sulphur cathode for lithium-sulphur batteries, Nature Mater. 8 (6) (2009) 500–506, http://dx.doi.org/10.1038/nmat2460.

[15] Z. Zhao-Karger, M.E. Gil Bardaji, O. Fuhr, M. Fichtner, A new class of non-corrosive, highly efficient electrolytes for rechargeable magnesium batteries, J. Mater. Chem. A 5 (22) (2017) 10815–10820, http://dx.doi.org/10.1039/c7ta02237a.

[16] B.P. Vinayan, Z. Zhao-Karger, T. Diemant, V.S.K. Chakravadhanula, N.I. Schwarzburger, M.A. Cambaz, R.J. Behm, C. Kübel, M. Fichtner, Performance study of magnesium-sulfur battery using a graphene based sulfur composite cathode electrode and a non-nucleophilic Mg electrolyte, Nanoscale 8 (6) (2016) 3296–3306, http://dx.doi.org/10.1039/c5nr04383b.

[17] J. Fanous, M. Wegner, J. Grimminger, Ä. Andresen, M.R. Buchmeiser, Structure-related electrochemistry of sulfur-poly(acrylonitrile) composite cathode materials for rechargeable lithium batteries, Chem. Mater. 23 (22) (2011) 5024–5028, http://dx.doi.org/10.1021/cm202467u.

[18] J. Fanous, M. Wegner, J. Grimminger, M. Rolff, M.B.M. Spera, M. Tenzer, M.R. Buchmeiser, Correlation of the electrochemistry of poly(acrylonitrile)–sulfur composite cathodes with their molecular structure, J. Mater. Chem. 22 (43) (2012) 23240, http://dx.doi.org/10.1039/c2jm34487d.

[19] T. Lebherz, M. Frey, A. Hintennach, M.R. Buchmeiser, Influence of morphology of monolithic sulfur-poly(acrylonitrile) composites used as cathode materials in lithium-sulfur batteries on electrochemical performance, RSC Adv. 9 (13) (2019) 7181–7188, http://dx.doi.org/10.1039/C8RA09976F.

[20] A. Mayer, M.R. Buchmeiser, Communication—Influence of temperature and electrolyte viscosity on the electrochemical performance of SPAN-based Lithium-Sulfur Cells, J. Electrochem. Soc. 165 (16) (2018) A3943–A3945, http://dx.doi.org/10.1149/2.0821816jes.

[21] P. Wang, J. Trück, S. Niesen, J. Kappler, K. Küster, U. Starke, F. Ziegler, A. Hintennach, M.R. Buchmeiser, High-performance Magnesium-Sulfur batteries based on a sulfurated poly(acrylonitrile) Cathode, a borohydride electrolyte, and a high-surface area magnesium anode, Batter. Supercaps 3 (11) (2020) 1239–1247, http://dx.doi.org/10.1002/batt.202000097.

[22] S. Warneke, A. Hintennach, M.R. Buchmeiser, Communication—Influence of carbonate-based electrolyte composition on cell performance of SPAN-based Lithium-Sulfur-Batteries, J. Electrochem. Soc. 165 (10) (2018) A2093–A2095, http://dx.doi.org/10.1149/2.0361810jes.

[23] T.N.L. Doan, M. Ghaznavi, Y. Zhao, Y. Zhang, A. Konarov, M. Sadhu, R. Tangirala, P. Chen, Binding mechanism of sulfur and dehydrogenated polyacrylonitrile in sulfur/polymer composite cathode, J. Power Sources 241 (2013) 61–69, http://dx.doi.org/10.1016/j.jpowsour.2013.04.113.

[24] R. Mukkabla, M.R. Buchmeiser, Cathode materials for lithium–sulfur batteries based on sulfur covalently bound to a polymeric backbone, J. Mater. Chem. A 8 (11) (2020) 5379–5394, http://dx.doi.org/10.1039/C9TA12619H.

[25] W. Wang, Z. Cao, G.A. Elia, Y. Wu, W. Wahyudi, E. Abou-Hamad, A.-H. Emwas, L. Cavallo, L.-J. Li, J. Ming, Recognizing the mechanism of sulfurized polyacrylonitrile Cathode materials for Li–S Batteries and beyond in Al–S Batteries, ACS Energy Lett. 3 (12) (2018) 2899–2907, http://dx.doi.org/10.1021/acsenergylett.8b01945.

[26] S. Wei, L. Ma, K.E. Hendrickson, Z. Tu, L.A. Archer, Metal–sulfur battery cathodes based on PAN–Sulfur composites, J. Am. Chem. Soc. 137 (37) (2015) 12143–12152, http://dx.doi.org/10.1021/jacs.5b08113.

[27] S. Warneke, M. Eusterholz, R.K. Zenn, A. Hintennach, R.E. Dinnebier, M.R. Buchmeiser, Differences in electrochemistry between fibrous SPAN and fibrous S/C cathodes relevant to cycle stability and capacity, J. Electrochem. Soc. 165 (1) (2018) A6017–A6020, http://dx.doi.org/10.1149/2.0061801jes.

[28] S. Ponnada, M.S. Kiai, D.B. Gorle, A. Nowduri, History and recent developments in divergent electrolytes towards high-efficiency lithium–sulfur batteries – a review, Mater. Adv. 2 (2021) 4115–4139, http://dx.doi.org/10.1039/D1MA00332A.

[29] J. Kappler, S.V. Klostermann, P.L. Lange, M. Dyballa, L. Veith, T. Schleid, T. Weil, J. Kästner, M.R. Buchmeiser, Sulfur-composites derived from poly(acrylonitrile) and poly(vinylacetylene) – a comparative study on the role of pyridinic and thioamidic nitrogen, Batter. Supercaps 6 (3) (2023) e202200522, http://dx.doi.org/10.1002/batt.202200522.

[30] S. Hein, T. Danner, D. Westhoff, B. Prifling, R. Scurtu, L. Kremer, A. Hoffmann, A. Hilger, M. Osenberg, I. Manke, M. Wohlfahrt-Mehrens, V. Schmidt, A. Latz, Influence of conductive additives and binder on the impedance of lithium-ion battery electrodes: Effect of morphology, J. Electrochem. Soc. 167 (1) (2020) 013546, http://dx.doi.org/10.1149/1945-7111/ab6b1d.

[31] D. Westhoff, T. Danner, S. Hein, R. Scurtu, L. Kremer, A. Hoffmann, A. Hilger, I. Manke, M. Wohlfahrt-Mehrens, A. Latz, V. Schmidt, Analysis of microstructural effects in multi-layer lithium-ion battery cathodes, Mater. Charact. 151 (2019) 166–174, http://dx.doi.org/10.1016/j.matchar.2019.02.031.

[32] V. De Lauri, L. Krumbein, S. Hein, B. Prifling, V. Schmidt, T. Danner, A. Latz, Beneficial effects of three-dimensional structured electrodes for the fast charging of lithium-ion batteries, ACS Appl. Energy Mater. 4 (12) (2021) 13847–13859, http://dx.doi.org/10.1021/acsaem.1c02621.

[33] T. Danner, M. Singh, S. Hein, J. Kaiser, H. Hahn, A. Latz, Thick electrodes for li-ion batteries: A model based analysis, J. Power Sources 334 (2016) 191–201, http://dx.doi.org/10.1016/j.jpowsour.2016.09.143.

[34] T. Knorr, S. Hein, B. Prifling, M. Neumann, T. Danner, V. Schmidt, A. Latz, Simulation-based and data-driven techniques for quantifying the influence of the carbon binder domain on electrochemical properties of li-ion batteries, Energies 15 (21) (2022) http://dx.doi.org/10.3390/en15217821.

[35] K. Kumaresan, Y. Mikhaylik, R.E. White, A mathematical model for a Lithium–Sulfur cell, J. Electrochem. Soc. 155 (8) (2008) A576, http://dx.doi.org/10.1149/1.2937304.

[36] M. Ghaznavi, P. Chen, Sensitivity analysis of a mathematical model of lithium-sulfur cells part I: Applied discharge current and cathode conductivity, J. Power Sources 257 (2014) 394–401, http://dx.doi.org/10.1016/j.jpowsour.2013.10.135.

[37] M. Ghaznavi, P. Chen, Sensitivity analysis of a mathematical model of lithium-sulfur cells: Part II: Precipitation reaction kinetics and sulfur content, J. Power Sources 257 (2014) 402–411, http://dx.doi.org/10.1016/j.jpowsour.2013.12.145.

[38] M. Ghaznavi, P. Chen, Analysis of a mathematical model of lithium-sulfur cells part III: Electrochemical reaction kinetics, transport properties and charging, Electrochim. Acta 137 (2014) 575–585, http://dx.doi.org/10.1016/j.electacta.2014.06.033.

[39] D.N. Fronczek, W.G. Bessler, Insight into lithium-sulfur batteries: Elementary kinetic modeling and impedance simulation, J. Power Sources 244 (2013) 183–188, http://dx.doi.org/10.1016/j.jpowsour.2013.02.018.

[40] T. Zhang, M. Marinescu, L. O'Neill, M. Wild, G. Offer, Modeling the voltage loss mechanisms in lithium-sulfur cells: The importance of electrolyte resistance and precipitation kinetics, Phys. Chem. Chem. Phys. 17 (35) (2015) 22581–22586, http://dx.doi.org/10.1039/c5cp03566j.

[41] T. Danner, G. Zhu, A.F. Hofmann, A. Latz, Modeling of nano-structured cathodes for improved lithium-sulfur batteries, Electrochim. Acta 184 (2015) 124–133, http://dx.doi.org/10.1016/j.electacta.2015.09.143.

[42] V. Thangavel, K.-H. Xue, Y. Mammeri, M. Quiroga, A. Mastouri, C. Guéry, P. Johansson, M. Morcrette, A.A. Franco, A microstructurally resolved model for li-s batteries assessing the impact of the cathode design on the discharge performance, J. Electrochem. Soc. 163 (13) (2016) A2817–A2829, http://dx.doi.org/10.1149/2.0051614jes.

[43] T. Danner, A. Latz, On the influence of nucleation and growth of S8 and Li2S in lithium-sulfur batteries, Electrochim. Acta 322 (2019) http://dx.doi.org/10.1016/j.electacta.2019.134719.

[44] M. Cornish, M. Marinescu, Toward rigorous validation of li-s battery models, J. Electrochem. Soc. 169 (6) (2022) 060531, http://dx.doi.org/10.1149/1945-7111/ac7750.

[45] T. Zhu, J.E. Mueller, M. Hanauer, U. Sauter, T. Jacob, Structural motifs for modeling sulfur-poly(acrylonitrile) composite materials in sulfur-lithium batteries, ChemElectroChem 4 (10) (2017) 2494–2499, http://dx.doi.org/10.1002/celc.201700428.

[46] T. Zhu, J.E. Mueller, M. Hanauer, U. Sauter, T. Jacob, Theoretical studies on the charging and discharging of poly(acrylonitrile)-based lithium-sulfur batteries, ChemElectroChem 4 (11) (2017) 2975–2980, http://dx.doi.org/10.1002/celc.201700549.

[47] C.-J. Huang, J.-H. Cheng, W.-N. Su, P. Partovi-Azar, L.-Y. Kuo, M.-C. Tsai, M.-H. Lin, S. Panahian Jand, T.-S. Chan, N.-L. Wu, P. Kaghazchi, H. Dai, P.M. Bieker, B.-J. Hwang, Origin of shuttle-free sulfurized polyacrylonitrile in lithium-sulfur batteries, J. Power Sources 492 (2021) 229508, http://dx.doi.org/10.1016/j.jpowsour.2021.229508.

[48] S. Perez Beltran, P.B. Balbuena, A solid electrolyte interphase to protect the sulfurized polyacrylonitrile (span) composite for li–s batteries: computational approach addressing the electrolyte/span interfacial reactivity, J. Mater. Chem. A 9 (2021) 7888–7902, http://dx.doi.org/10.1039/D1TA00110H.

[49] S. Perez Beltran, P.B. Balbuena, Sulfurized polyacrylonitrile (span): Changes in mechanical properties during electrochemical lithiation, J. Phys. Chem. C 125 (24) (2021) 13185–13194, http://dx.doi.org/10.1021/acs.jpcc.1c02966.

[50] W. Wang, Z. Cao, G.A. Elia, Y. Wu, W. Wahyudi, E. Abou-Hamad, A.H. Emwas, L. Cavallo, L.J. Li, J. Ming, Recognizing the mechanism of sulfurized polyacrylonitrile cathode materials for Li-S batteries and beyond in Al-S Batteries, ACS Energy Lett. 3 (12) (2018) 2899–2907, http://dx.doi.org/10.1021/acsenergylett.8b01945.

[51] X. Wang, Y. Qian, L. Wang, H. Yang, H. Li, Y. Zhao, T. Liu, Sulfurized polyacrylonitrile cathodes with high compatibility in both ether and carbonate electrolytes for ultrastable Lithium–Sulfur batteries, Adv. Funct. Mater. 29 (39) (2019) 1902929, http://dx.doi.org/10.1002/adfm.201902929.

[52] S. Zhang, Understanding of sulfurized polyacrylonitrile for superior performance Lithium/Sulfur Battery, Energies 7 (7) (2014) 4588–4600, http://dx.doi.org/10.3390/en7074588.
[53] S.V. Klostermann, J. Kappler, A. Waigum, M.R. Buchmeiser, A. Köhn, J. Kästner, The reduction behavior of sulfurized polyacrylonitrile (span) in lithium–sulfur batteries using a carbonate electrolyte: a computational study, Phys. Chem. Chem. Phys. (2024) http://dx.doi.org/10.1039/D3CP06248A.
[54] Y. Wu, M. Yang, Y. Zou, S. Wang, S. Hou, B. Hu, C. Yang, Y. Tao, A novel crosslinked sulfur-containing polymer cathode material for high-performance lithium-sulfur batteries, Electrochim. Acta 427 (2022) 140890, http://dx.doi.org/10.1016/j.electacta.2022.140890.
[55] J. Luo, Z. Chen, R. Zhang, C. Lu, J. Zhu, X. Zhuang, Realizing sulfurized polyacrylonitrile cathode in ether-based electrolyte, Electrochim. Acta 474 (2024) 143533, http://dx.doi.org/10.1016/j.electacta.2023.143533.
[56] S. Bertolini, T. Jacob, Atomistic discharge studies of sulfurized-polyacrylonitrile through ab initio molecular dynamics, Electrochim. Acta 403 (2022) 139538, http://dx.doi.org/10.1016/j.electacta.2021.139538.
[57] T. Yim, M.-S. Park, J.-S. Yu, K.J. Kim, K.Y. Im, J.-H. Kim, G. Jeong, Y.N. Jo, S.-G. Woo, K.S. Kang, I. Lee, Y.-J. Kim, Effect of chemical reactivity of polysulfide toward carbonate-based electrolyte on the electrochemical performance of li–s batteries, Electrochim. Acta 107 (2013) 454–460, http://dx.doi.org/10.1016/j.electacta.2013.06.039.
[58] R. Richter, J. Häcker, Z. Zhao-Karger, T. Danner, N. Wagner, M. Fichtner, K.A. Friedrich, A. Latz, Degradation effects in Metal-Sulfur Batteries, ACS Appl. Energy Mater. 4 (3) (2021) 2365–2376, http://dx.doi.org/10.1021/acsaem.0c02888.
[59] M.Z. Bazant, Theory of chemical kinetics and charge transfer based on nonequilibrium thermodynamics, Acc. Chem. Res. 46 (5) (2013) 1144–1160, arXiv:1208.1587.
[60] A. Latz, J. Zausch, Thermodynamic derivation of a Butler-Volmer model for intercalation in Li-ion batteries, Electrochim. Acta 110 (2013) 358–362, http://dx.doi.org/10.1016/j.electacta.2013.06.043.
[61] V. Deimede, C. Elmasides, Separators for lithium-ion batteries: A review on the production processes and recent developments, Energy Technol. 3 (5) (2015) 453–468, http://dx.doi.org/10.1002/ente.201402215.
[62] X. Huang, Separator technologies for lithium-ion batteries, J. Solid State Electrochem. 15 (4) (2011) 649–662, http://dx.doi.org/10.1007/s10008-010-1264-9.
[63] P. Arora, Z.J. Zhang, Battery separators, Chem. Rev. 104 (10) (2004) 4419–4462, http://dx.doi.org/10.1021/cr020738u, publisher: American Chemical Society.
[64] R. Raccichini, L. Furness, J.W. Dibden, J.R. Owen, N. García-Araez, Impedance characterization of the transport properties of electrolytes contained within porous electrodes and separators useful for li-s batteries, J. Electrochem. Soc. 165 (11) (2018) A2741, http://dx.doi.org/10.1149/2.0631811jes.
[65] H. Lundgren, M. Behm, G. Lindbergh, Electrochemical characterization and temperature dependency of mass-transport properties of $lipf_6$ in ec:dec, J. Electrochem. Soc. 162 (3) (2014) A413–A420, http://dx.doi.org/10.1149/2.0641503jes.
[66] F. Tuerxun, Y. Abulizi, Y. NuLi, S. Su, J. Yang, J. Wang, High concentration magnesium borohydride/tetraglyme electrolyte for rechargeable magnesium batteries, J. Power Sources 276 (2015) 255–261, http://dx.doi.org/10.1016/j.jpowsour.2014.11.113.
[67] J. Landesfeind, H.A. Gasteiger, Temperature and concentration dependence of the ionic transport properties of lithium-ion battery electrolytes, J. Electrochem. Soc. 166 (14) (2019) A3079–A3097, http://dx.doi.org/10.1149/2.0571912jes.
[68] S. Niesen, J. Trück, C. Seidl, K. Renger, M.R. Buchmeiser, Lithium-sulfur batteries based on sulfurized poly(acrylonitrile) cathodes: impact of electrode density on cell performance, J. Electrochem. Soc. 168 (11) (2021) 110513, http://dx.doi.org/10.1149/1945-7111/ac334d.
[69] J. Liu, Z. Bao, Y.e.a. Cui, Pathways for practical high-energy long-cycling lithium metal batteries, Nat. Energy 4 (2019) 180–186, http://dx.doi.org/10.1038/s41560-019-0338-x.
[70] L. Yu, S. Chen, H. Lee, L. Zhang, M.H. Engelhard, Q. Li, S. Jiao, J. Liu, W. Xu, J.-G. Zhang, A localized high-concentration electrolyte with optimized solvents and lithium difluoro(oxalate)borate additive for stable lithium metal batteries, ACS Energy Lett. 3 (9) (2018) 2059–2067, http://dx.doi.org/10.1021/acsenergylett.8b00935.
[71] P. Delahay, C.W. Tobias, Advances in Electrochemistry and Electrochemical Engineering, in: electrochemical engineering, Vol. 8, 1971.
[72] K.K. Patel, J.M. Paulsen, J. Desilvestro, Numerical simulation of porous networks in relation to battery electrodes and separators, J. Power Sources 122 (2) (2003) 144–152, http://dx.doi.org/10.1016/S0378-7753(03)00399-9.
[73] J. Landesfeind, J. Hattendorff, A. Ehrl, W.A. Wall, H.A. Gasteiger, Tortuosity determination of battery electrodes and separators by impedance spectroscopy, J. Electrochem. Soc. 163 (7) (2016) A1373, http://dx.doi.org/10.1149/2.1141607jes.